Two mechanisms of Josephson phase shift generation by an Abrikosov vortex

T. Golod,[1] A. Pagliero,[1] and V. M. Krasnov[1,2,*]

[1]*Department of Physics, Stockholm University, AlbaNova University Center, SE-10691 Stockholm, Sweden*

[2]*Moscow Institute of Physics and Technology, State University, 9 Institutskiy per., Dolgoprudny, Moscow Region 141700, Russia*

(Received 28 August 2019; published 11 November 2019)

Abrikosov vortices contain magnetic fields and circulating currents that decay at a short range $\lambda \sim 100$ nm. However, vortices can induce Josephson phase shifts at a long range $r \sim \mu\text{m} \gg \lambda$. Mechanisms of this puzzling phenomenon are not clearly understood. Here we present a systematic study of vortex-induced phase shifts in planar Josephson junctions. We make two key observations: (i) The cutoff effect: Although vortex-induced phase shift is a long-range phenomenon, it is terminated by the junction and does not persist beyond it. (ii) A linear to superlinear crossover with a rapid upturn of the phase shift occurs upon approaching a vortex to a junction. The crossover occurs at a vortex-junction distance comparable to the penetration depth. Together with theoretical and numerical analysis this allows unambiguous identification of two distinct and independent mechanisms. The short range $r \lesssim \lambda$ mechanism is due to circulating vortex currents *inside* a superconducting electrode without involvement of magnetic fields. The long range $r \gg \lambda$ mechanism is due to stray magnetic fields *outside* electrodes without circulating vortex currents. We argue that understanding of controlling parameters of vortex-induced Josephson phase shift can be used for development of novel compact cryoelectronic devices.

DOI: 10.1103/PhysRevB.100.174511

I. INTRODUCTION

Josephson electronics operate with a quantum-mechanical Josephson phase difference (JPD), φ, between two superconducting electrodes. In conventional Josephson junctions (JJ's) $\varphi = 0$ in the absence of applied currents and is spatially independent, $\varphi(x) = \text{const}$, without external magnetic fields. It is anticipated that unconventional junctions with either a fixed spatially independent JPD (φ junctions) or a spatially dependent Josephson phase shift (JPS) along the junction (0-φ junctions) may provide additional functionality in Josephson electronics [1–4]. For example, they can operate as autonomous and persistent phase batteries—one of key elements of quantum [1,5–14] and digital Josephson electronics [2,3,15,16]. Such junctions can also be used for development of novel types of cryogenic memory [17–22]. A π shift is most commonly needed, e.g., for bringing flux qubits to a degeneracy point [1,5–7], for realization of complementary digital electronics [2,3,15,16], and for maximum distinction between 0 and 1 state in memory cells [17].

Several ways of making φ and 0-φ junctions are known. 0-φ junctions can be created via self-field effect, which is induced by uneven distribution of critical or bias currents [23–27] and affects the dynamics of Josephson vortices [23,24,28]. π junctions with a fixed JPD, $\varphi = \pi$, can be realized using hybrid superconductor/ferromagnet (S/F) structures [29–31] and unconventional superconductors with sign-reversal order parameter, e.g., d wave [2,32,33], or $s_{\pm}$ [34–37]. φ junctions with arbitrary JPD can be made using inhomogeneous S/F junctions [38,39] or junctions with strong spin-orbit coupling [40]. JPD in the above-mentioned junctions is either persistent but not tunable (e.g., SFS junctions and junctions with sign-reversal order parameter), or tunable but not persistent (e.g., 0-φ junctions based on uneven current injection [25]).

Abrikosov vortex (AV), with a 2π rotation of the phase of superconducting order parameter can also induce JPS in a nearby JJ [41–46]. AV-induced JPS depends on the distance and geometry [43,44]. AV can be easily and controllably manipulated (displaced, introduced, or removed) by magnetic field [43,47], current [17,47,48], light, or heat [46,49] pulses. Therefore, vortices can be used for creation of memory cells [17] and tunable but persistent phase batteries.

At present, the mechanism of AV-induced JPS is still not well understood. Circulating currents and magnetic fields of AV decay exponentially at a short range given by the London penetration depth $\lambda \sim 100$ nm. However, AV-induced JPS is decaying much slower and persists at distances of a few microns [43]. To some extent it resembles a long-range Aharonov-Bohm effect [50]. For example, there is a seeming direct relation between JPS and rotation of the phase of superconducting order parameter inside the vortex, given by the polar angle Θ [43]. Yet, it cannot be the Aharonov-Bohm effect because phase variation at a line segment (junction length) is not a gauge-invariant quantity and cannot have physical significance. Although the problem of AV-induced JPS has been considered theoretically in several previous publications and has been solved in some limiting cases [41,42,44–46], at present there is neither a qualitative understanding of the long-range nature of the phenomenon, nor a quantitative description of AV-induced JPS for realistic sample geometries.

Here we perform a systematic analysis of vortex-induced Josephson phase shifts in Nb-based planar Josephson junctions with artificial vortex traps. We observe that although AV-induced JPS is a long-range phenomenon, it is terminated

*Vladimir.Krasnov@fysik.su.se

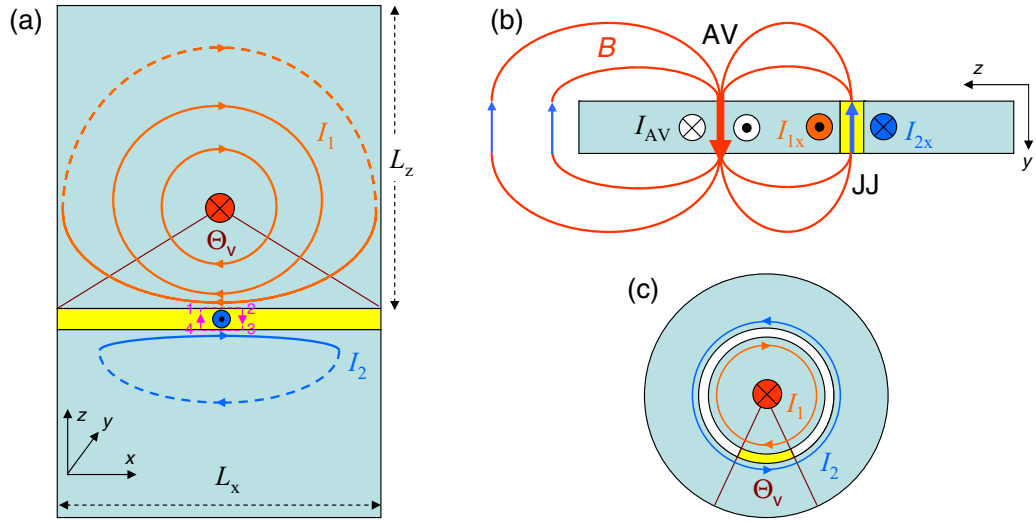

FIG. 1. Sketches of considered vortex-junction configurations. (a) A top view of planar junction (yellow region) with trapped Abrikosov vortex in the first (top) electrode. Lines indicate current streamlines. (b) A side view of the same configuration. Lines indicate magnetic field lines of vortex stray fields. (c) A top view of Corbino disk geometry, in which the fraction of stray flux entering the junction is proportional to the polar angle of the vortex within the junction segment Θ_v.

(cutoff) by the junction and does not persist beyond it. Distance dependence of the JPS revealed a linear to superlinear crossover with a rapid upturn of JPS. The crossover occurs at AV-JJ distance comparable to the penetration depth. This allows unambiguous identification of two distinct and independent mechanisms of AV-induced JPS. The short range mechanism is due to circulating vortex currents *inside* superconducting electrodes without involvement of magnetic fields. The long-range mechanism is due to stray magnetic fields *outside* electrodes without circulating vortex currents. It is long range because stray fields cannot enter the superconductor and can spread out along the surface up to arbitrary long distances. Our conclusions are supported by numerical simulations and theoretical analysis, which also provides a general vortex-image solution for the current-induced JPS. We argue that the detailed understanding of geometrical factors controlling the vortex-induced Josephson phase shift facilitates development of novel vortex-based cryoelectronic devices.

II. THEORETICAL ANALYSIS

Let's consider a single AV in one of the electrodes of a planar JJ, see a sketch in Fig. 1(a). We assume that the junction is short, i.e., its length L_x is smaller than double the Josephson penetration depth λ_J. The vortex has a 2π phase rotation, clockwise circulating currents and magnetic flux, decaying at some characteristic scale λ^* *inside* the superconducting electrode. In the limiting cases of a thick electrode, $d \gg \lambda$, it is equal to the London penetration depth, $\lambda^* = \lambda$. For thin films, $d \ll \lambda$ it is given by the Pearl length $\lambda^* = \lambda^2/d$ [51]. Finally, there are stray fields from the vortex *outside* electrodes. They cannot enter the superconducting electrode and, therefore, stretch along its surface until edges, where they eventually close, as sketched in Fig. 1(b). In this section we discuss how four vortex-related factors, phase rotation of the superconducting condensate, circulating currents, inner vortex fields, and outer stray fields, contribute to JPD.

As reported earlier [43], the value and the sign of AV-induced JPS can be estimated using a naive assumption of rigid 2π phase rotation around the vortex (the London gauge). In this case JPD is just equal to the polar angle,

$$\varphi_v(x) = -V \arctan\left(\frac{x - x_v}{|z_v|}\right), \tag{1}$$

where V is the vorticity ($+1$ for a vortex, -1 for an antivortex), x_v is the coordinate of the vortex along the junction and z_v is the distance to the junction. The total JPS within the junction, $\Delta\varphi_v = \varphi_v(L_x) - \varphi_v(x = 0)$, is equal to the polar angle of the vortex within the junction segment Θ_v, indicated in Fig. 1(a), $\Delta\varphi_v \simeq \Theta_v = \arctan[x_v/|z_v|] + \arctan[(L_x - x_v)/|z_v|]$. The sign of the phase shift is determined by the direction of phase rotation. In Fig. 1(a) we sketch the case of a vortex (clockwise rotation) in the top electrode. Since φ is the difference of phases of top and bottom electrodes, a vortex induces negative JPS $\Delta\varphi_v < 0$, irrespective of in which electrode it is placed. Indeed, when it is placed in the top electrode, it induces a negative phase gradient solely in the top electrode. But if we translate it to the bottom electrode it will induce a positive phase gradient solely in the bottom electrode. This explains the minus sign and the absolute value $|z_v|$ in Eq. (1). However, as we already mentioned, rigid phase rotation cannot provide a proper explanation of AV-induced JPS because phase of the condensate is not a gauge-invariant quantity and cannot acquire a physically significant value at a line segment (junction length). Therefore, JPS has to be induced by circulating currents and fields of the vortex.

Within linear electrodynamics (neglecting spatial variation of the order parameter), current densities $J_{1,2}$ in the two electrodes are described by the generalized second London equation:

$$J_{1,2} = \frac{c}{4\pi\lambda_{1,2}^2}\left[\frac{\Phi_0}{2\pi}\nabla\eta_{1,2} - A\right]. \tag{2}$$

Here η and A are the corresponding scalar (phase) and vector potentials. The gauge-invariant JPD is obtained by integration of Eq. (2) over an infinitesimal contour 1-2-3-4, see Fig. 1(a), covering the barrier:

$$\frac{1}{2\pi}\frac{\partial\varphi}{\partial x} = \frac{4\pi\lambda_{1,2}^2}{\Phi_0 c}(J_{1x} - J_{2x}) + \frac{t}{\Phi_0}B_y. \tag{3}$$

Here t is the width of the barrier, $J_{1,2x}$ are x components in the vicinity of the barrier, B_y is the y component of magnetic induction in the barrier. In the Meissner state (no vortices), $J_{1,2x}$ can be obtained explicitly by solving Eq. (2) in the electrodes, with boundary conditions $B_y = H$ outside the junction (H is applied external field in the y direction). A straightforward calculation yields [52]:

$$\frac{\partial\varphi_M}{\partial x} = \frac{2\pi d_{\text{eff}}}{\Phi_0}B_y, \tag{4}$$

where d_{eff} is the effective magnetic thickness of the junction. For sandwich-type JJs d_{eff} is determined by λ, but for planar JJs, studied below, d_{eff} is determined by sizes $L_{x,z}$ of junction electrodes [27,53–56]. Integration of Eq. (4) over the junction length $x \in [0, L_x]$ provides an explicit expression for the field-induced JPS:

$$\Delta\varphi_M = 2\pi\frac{\Phi}{\Phi_0}, \tag{5}$$

where $\Phi = d_{\text{eff}}\int_0^{L_x} B_y dx$ is the total flux in the junction.

Due to linearity of London electrodynmics, JPD in the presence of a vortex is a superposition of the Meissner contribution at a given H and vortex-induced contribution at zero field:

$$\varphi = \varphi_M(H) + \varphi_v(H = 0). \tag{6}$$

Vortex currents and fields contribute differently to JPS. For example, in the mesoscopic case $L_x \ll \lambda^*$, the total flux carried by the vortex $\Phi_v \sim (L_x/\lambda^*)^2\Phi_0 \ll \Phi_0$ becomes negligible [52]. Thus, there is no magnetic field neither inside nor outside the vortex and current makes the only contribution to the phase shift. All previous theoretical studies considered similar cases without field contribution to vortex-induced JPS [41,42,44–46]. We note that junctions studied here and earlier [17,43] have intermediate electrode thickness $d \sim \lambda$ [53] and electrode sizes $L_x \sim$ 5–6 μm significantly larger than $\lambda^* \sim$ 100–300 nm. Therefore, stray fields cannot be neglected in our experiment. Below we will consider both limiting cases $r \ll \lambda^*$ and $r \gg \lambda^*$.

A. Current induced mechanism in a mesoscopic limit, $L_x \ll \lambda^*$

Let's first consider the mesoscopic case $L_x \ll \lambda^*$. In this case vortex flux $\Phi \simeq 0$ and all magnetic field effects can be neglected. Therefore, Eq. (2) can be rewritten in cylindrical (r, Θ) coordinates as

$$rotJ = \frac{c\Phi_0}{4\pi\lambda^{*2}}\delta(\Theta), \tag{7}$$

where r is the distance from the vortex, Θ is the polar angle, and $\delta(\Theta)$ is a delta function. Direct integration yields

$$J_\Theta = \frac{c\Phi_0}{8\pi^2\lambda^{*2}}\frac{1}{r}. \tag{8}$$

Since $B_y = 0$, there are no field-induced screening currents in the second electrode, $J_{2x} = 0$. If we substitute J_{1x} from Eq. (8) into Eq. (3), we obtain $\varphi_v = \Theta$, which is equivalent to Eq. (1). However, this is not a self-consistent solution because Eq. (8) does not take into account a boundary condition that currents cannot cross electrode edges [57]. This leads to distortion of stream lines, as sketched in Fig. 1(a).

The boundary condition can be accounted for using a well known image method [42]. A mirror image with reverse vorticity should be added at the other side of the edge. It cancels out the perpendicular component of the current through this edge. However, it adds a smaller current at the opposite edge. To compensate it an image of an image should be introduced at the opposite edge, and so on. This leads to an infinite series of images due to reflections from all the edges, as illustrated in Fig. 2(a). Each image vortex generates JPD $\varphi_v(x_n, z_m)$ according to Eq. (1) with image vortex coordinates (x_n, z_m) and corresponding vorticity V_{nm}. The image solution for AV-induced JPD is then

$$\varphi_v = \sum_{n,m}\varphi_v(x_n, z_m), \tag{9}$$

where the sum is taken over the image array. It is rapidly converging and can be easily calculated, as described in Appendix A. For a semi-infinite electrode, $L_z = \infty$, the image array consists of the primary image row I due to reflections from left and right edges, and an antirow I′ due to mirror reflection from the bottom (junction) edge, see Fig. 2(a). The green line in Fig. 2(b) shows corresponding antivortex induced JPS as a function of vortex polar angle Θ_v. Simulations are made for a vortex at $x_v = 0.5L_x$ and for varying z_v, see a sketch in the inset of Fig. 2(b). $\Theta_v = 0$ corresponds to vortex-free case $z_v = \infty$ and $\Theta_v \simeq \pi$ to AV at the edge of the junction $z_v \to 0$.

In Ref. [44] J. Clem obtained a self-consistent solution for Pearl vortex-induced JPS in thin film planar JJ with narrow long electrodes ($d \ll \lambda$, $L_x \ll \lambda_P$, $L_z = \infty$). The solution is described in Appendix B. It is shown by the dashed magenta line in Fig. 2(b). Apparently it coincides with the image array solution. The coincidence is not occasional because in the considered flux-free mesoscopic case the only vortex feature is the delta-function phase singularity, Eq. (7), irrespective of the vortex type (Pearl or Abrikosov). Consequently, the solutions are also identical.

From Fig. 2(b) it is seen that a vortex far away from the junction, $\Theta_v \simeq 0$, does not induce JPS, $\Delta\varphi_v \simeq 0$. Upon approaching to the junction, JPS increases and reaches the maximum value $\Delta\varphi_v = 2\pi$ when the vortex is at the edge of the junction, $\Theta_v = \pi$. Doubling of JPS with respect to Θ_v is due to concentration of currents in a narrow gap between the vortex and the junction. It can be viewed as an additional current from the image antivortex, which doubles the JPS. This doubling is quite peculiar. The total phase shift around the vortex is always 2π. However, at $z_v \to 0$ all of it is concentrated at one point at the nearest edge, in a stark contrast to a naive picture of rigid phase rotation around the vortex. Curiously, if we would make junctions at all the edges of vortex-carrying electrode, all other junctions except the one at which the vortex is placed would not show any phase shifts in this case. Below we will perform a similar experiment—simultaneous detection of the phase shift from

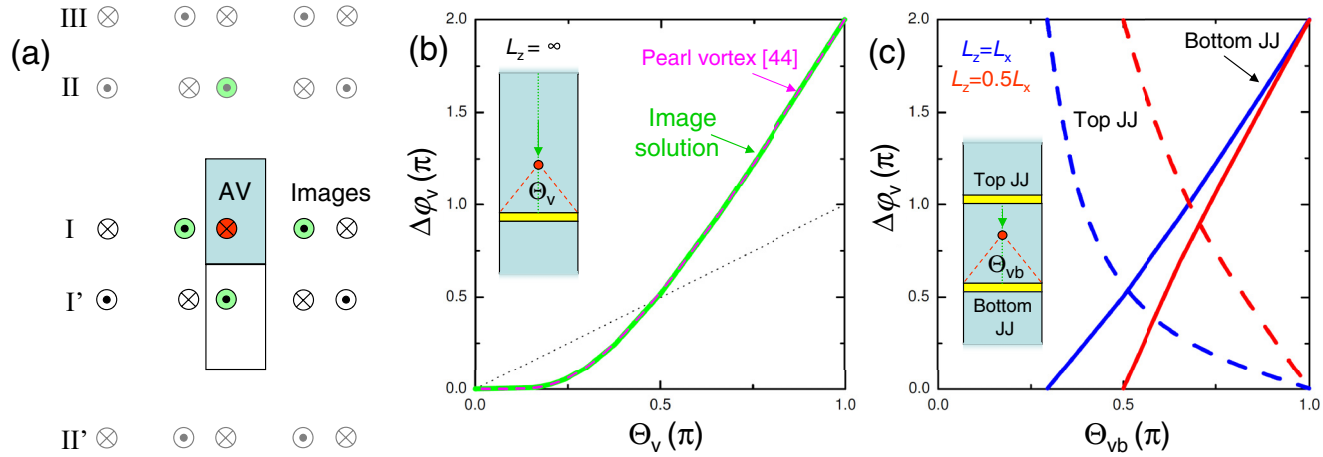

FIG. 2. (a) Illustration of an image solution for a rectangular electrode with a vortex. Green circles represent primary images from the four edges. Multiple mirror reflections from all edges lead to an infinite series of image vortices and antivortices. (b) Calculated variation of the vortex-induced JPS versus vortex polar angle for a junction with narrow $L_x \ll \lambda^*$, long $L_z = \infty$ electrodes. Calculations are made for an antivortex approaching the junction at $x_v = 0.5L_x$ from $z_v = \infty$ ($\Theta_v = 0$) to $z_v = 0$ ($\Theta_v = \pi$), as sketched in the inset. Green line represents the image array solution, which coincides with the solution from Ref. [44] for a Pearl antivortex (dashed magenta line). Black dotted line represents linear dependence $\Delta\varphi_v = \Theta_v$. (c) Image-array solutions for finite-size rectangular-shape electrodes with $L_z = L_x$ (blue lines) and $L_z = L_x/2$ (red lines). Here we consider a double junction experiment, sketched in the inset, and show a variation of JPS in the bottom (solid lines) and top (dashed lines) junctions made at the upper and lower edges of the electrode, versus the polar angle in the bottom junction, Θ_{vb}. Calculations are made for an antivortex moving at $x_v = 0.5L_x$ from the top, $z_v = L_z$ (minimal value of Θ_{vb}), to the bottom, $z_v = 0$ ($\Theta_{vb} = \pi$), junction, as sketched in the inset.

different sides of the vortex. This, however, could be done only for a finite-size (L_z) electrode. Subsequent reflections from bottom and top edges in the case of finite L_z electrode lead to the appearance of an infinite series of image rows I, I′, II, II′, III, e.t.c, as sketched in Fig. 2(a) (see Appendix A for details).

Inset in Fig. 2(c) shows a sketch of the double-junction experiment, which we will perform below. In this case the antivortex is placed in the middle electrode with two JJ's on top and bottom edges. Solid and dashed lines in Fig. 2(c) show image solutions in the bottom, $\Delta\varphi_{vb}$, and top, $\Delta\varphi_{vt}$, JJ's, respectively, versus polar angle in the bottom JJ, Θ_{vb}. Blue lines correspond to a square-shaped electrode, $L_z = L_x$, and red lines to a rectangular shape, $L_z = 0.5L_x$. It can be seen that upon moving of the vortex from one JJ to another the phase shift changes from 2π to 0 in the former and from 0 to 2π in the latter.

The disproportional to polar angle variation of JPS, compare green and black dotted lines in Fig. 2(b), is characteristic for the considered mesoscopic case. It is associated with nonlinearity (singularity) of current distribution around the vortex center, Eq. (8). Therefore, this disproportionality can be considered as a signature of the circulating current mechanism of JPS. Finally, we note that although JPS in this limit is decaying in a long-range manner $\propto 1/r$, see Eqs. (1) and (8), this is not a long range phenomenon because it is valid only at $r \ll \lambda^*$. In principle, the image method would be valid also for $r > \lambda^*$, provided there are no stray fields [41,42,46]. This is the case for elongated objects with zero demagnetization factor, but we will not discuss it further because it is not relevant for the considered case of planar thin-film junctions [17,43] and because this effect is rapidly decaying at $r > \lambda^*$ [41] and becomes insignificant at longer scales.

B. Stray-field mechanism in macroscopic junctions, $L_x \gg \lambda^*$

Next we consider an opposite limit, $L_x \gg \lambda^*$, which is usually the case for JJ's. In this case AV carries the full flux quantum and magnetic field effects are essential. If the vortex-junction distance is (much) larger than the effective penetration depth, $z_v > \lambda^*$, we may neglect circulating vortex currents at the junction. Similarly, we may neglect associated vortex fields *inside* the superconducting electrode. In this case vortex stray fields *outside* electrodes make the only contribution to JPS. Since stray fields cannot enter the superconductor, they have to spread along its surface until edges, as sketched in Fig. 1(b). The range of spreading is determined entirely by electrode geometry and can be very long.

When vortex stray fields reach the junction, the corresponding fraction of the flux closes through the junction, as sketched in Fig. 1(b). This creates an actual magnetic field in the junction with the sign opposite to that of the vortex. This field is large because of a flux-focusing effect caused by a large demagnetization factor of a thin film in perpendicular field [27]. It induces correspondingly large edge currents $I_{1x,2x}$ in the junction banks, which have equal amplitudes but opposite directions, $I_{1x} = -I_{2x}$, as sketched in Fig. 1(a). We want to emphasize the principle difference between circulating currents of the vortex, which are bulk (flow in the whole film thickness) and short-range $r \sim \lambda^*$, and stray-field induced surface currents, whose range is determined by the geometry of electrodes. In Fig. 1(b) we tried to separate them by painting short-range bulk vortex currents in black/white

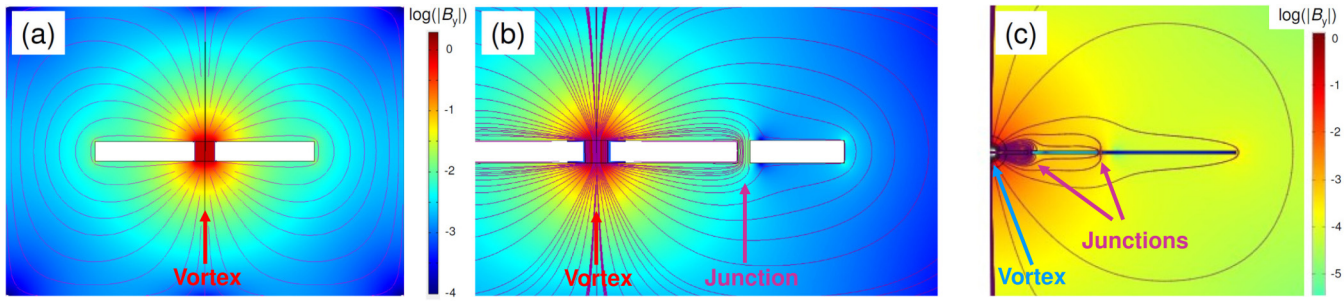

FIG. 3. 3D numerical simulations of stray field distribution from a vortex in a system of planar superconducting electrodes. We show side views through a central cross section containing the vortex (red spot with high field). White horizontal bands represent superconducting electrodes with $B = 0$. (a) Vortex in the center of a single square-shaped electrode (no junction). (b) For two electrodes, forming a single junction. (c) For three electrodes forming two planar junctions. Here the vortex is at the left edge of the panel and it is placed in the same square shaped electrode as in (a) (left part of the electrode is not shown). From panels (b) and (c) it can be seen that stray fields are predominantly closing through the nearest junction and that only a minor fraction reaches the outmost junction (note the logarithmic scale). This is consistent with the cutoff phenomenon observed in experiment.

and long-range stray-field-induced currents in orange/blue. In the limit considered here, $L_{x,z} \gg \lambda^*$, only stray-field-induced surface currents are present at the junction banks.

JPS induced by stray fields is given by Eq. (5), where Φ is the total stray flux closing through the junction. Since electrodes have a large area, $L_{x,z} \gg \lambda^*$, all the field reaching the junction goes in it because the penalty for stretching stray fields further is too high. The stray flux can be calculated exactly for the Corbino disk geometry, see Fig. 1(c), with a junction being a segment of the circle (painted yellow). In this case, due to the rotational symmetry, stray flux in the junction is $\Phi = (\Theta_v/2\pi)\Phi_0$ and, thus,

$$\Delta\varphi_v = \Theta_v, \tag{10}$$

consistent with Eq. (1).

Finding distribution of currents and stray fields in realistic planar junctions with large demagnetization factors is a complex three-dimensional problem, which can be solved only numerically. Figure 3 represents corresponding 3D simulations performed using COMSOL Multiphysics software. Superconductor is modelled as a material with zero magnetic permeability, leading to $B = 0$ inside junction electrodes [white horizontal bands in Figs. 3(a) and 3(b)]. The vortex is modeled by setting a finite magnetic field in the vortex trap (red spots with large field). We represent data in logarithmic scale so that color scales represent $\log_{10}(|B_y|)$ and densities of field lines represent $\log_{10}(|B|)$.

Figure 3(a) shows a side view of stray field distribution from a vortex in the center of square shaped superconducting film. In Fig. 3(b) a second electrode is added to the right of the initial electrode. The gap between the two electrodes represents a junction. It is seen that upon reaching the junction, stray fields are mostly penetrating into it and only a very small fraction reaches the right edge of the junction. Simulation in Fig. 3(c) represents the case with a third wider electrode added to the right, thus forming two junctions. It can be seen that most stray field lines are closed in the nearest junction and very few are expanding further out (note the logarithmic scale). Incomplete closing of stray fields in the nearest junction in our simulations is a consequence of a too small demagnetization factor (scaling with $L_{x,z}/d$) that we had to adopt for making a reasonably coarse mesh, to solve the problem on a personal computer. Planar junctions, studied below, have a much larger $L_{x,z}/d \sim 100$, with proportionally larger penalty for stretching stray fields to the outmost edge.

We checked that the stray flux (and thus JPS) in the junction is approximately proportional to Θ_v. This indicates a uniform radial spreading of vortex stray fields. Therefore, in the considered limit of a macroscopic junction $L_{x,z} \gg \lambda^*$ and for $z_v \gg \lambda^*$ the phase shift is induced solely by stray fields, proportionally to the polar angle, Eq. (1).

To summarize this section, there are two distinct contributions to vortex-induced JPS. The current-induced mechanism is short-range $r \lesssim \lambda^*$. The corresponding JPS is given by the image solution and is disproportional with respect to Θ_v. The stray field mechanism is long-range $r \sim L_z \gg \lambda^*$ and the corresponding JPS is approximately proportional to Θ_v. Despite quantitative differences, JPS for both mechanisms appear to be qualitatively similar and decay in a long-range manner as $1/r$. This is demonstrated in Fig. 4(a), which shows calculated JPS for the two mechanisms. Thick lines represent an image solution [Eq. (A2) from Appendix A, which coincides with the Pearl-vortex solution Eq. (B1) from Appendix B]. Thin lines represent the stray field contribution equal to the polar angle, Eq. (1), scaled to the same total phase shift. Apparently, the curves have similar shapes with only a minor difference at the edges due to different boundary conditions. The circulating current mechanism requires zero phase gradient at the edges because there is neither current through the edge, nor magnetic field in the corresponding mesoscopic limit. For the stray-field mechanism there is a finite field in the junction, which leads to a finite gradient at the edges, Eq. (4). Both effects are terminated at the junction because neither circulating currents nor stray fields persist beyond it. Therefore, only different ranges and functional dependencies $\Delta\varphi_v(\Theta_v)$ provide a possibility to discriminate the two mechanisms.

C. Numerical analysis of $I_c(H)$ patterns

Appearance of vortex-induced JPS leads to distortion of $I_c(H)$ patterns [17,43,44]. The critical current I_c corresponds

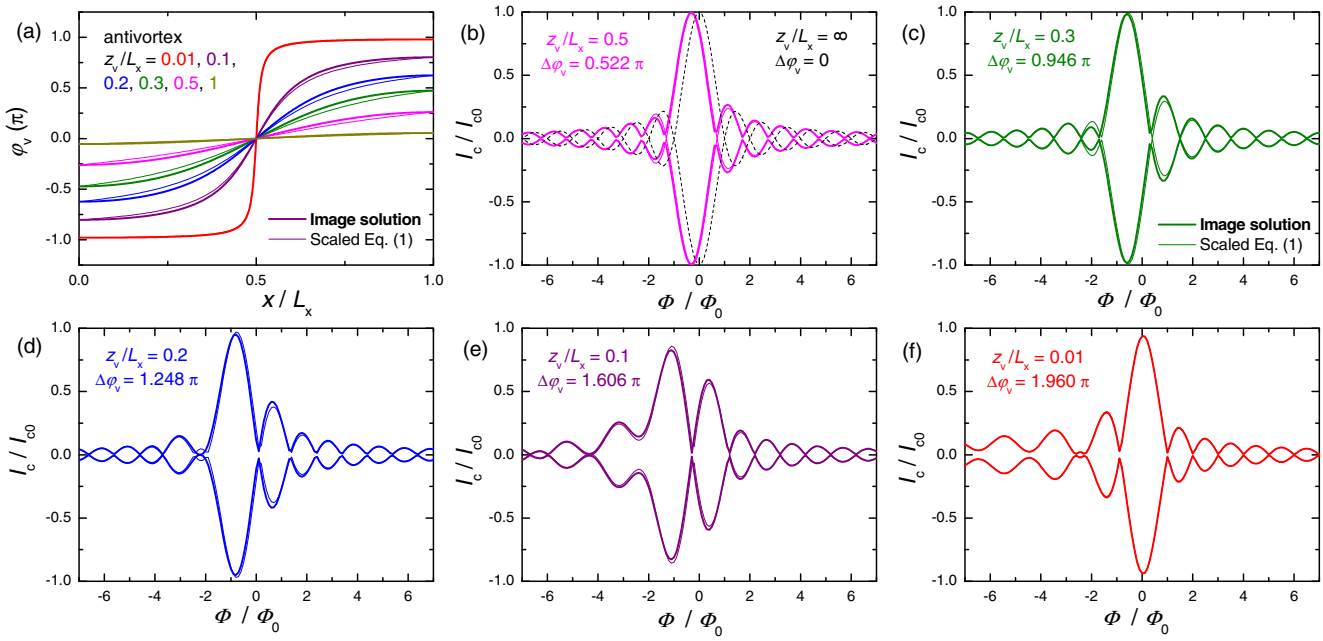

FIG. 4. Numerical modeling of $I_c(H)$ patterns for different distances z_v between junction and vortex. Simulations are made for an antivortex at different z_v and $x_v = 0.5L_x$ for a long $L_z = \infty$ electrode. (a) Phase shifts calculated from image array solution (thick lines) and Eq. (1), scaled to the same amplitude $\Delta\varphi_v$ (thin lines). (b)–(f) Variation of $I_c(H)$ patterns upon approaching of the antivortex to the junction. Dashed black line in (b) represents the vortex-free Fraunhofer pattern. Thick and thin lines in (b)–(f) are obtained for corresponding lines from (a). The difference is marginal.

to the maximum of Josephson current, $I = I_{c0}\sin(\varphi(x))$, integrated over the junction length, with $\varphi(x)$ given by Eq. (6). Figures 4(b)–4(f) show successive evolution of $I_c(H)$ patterns upon approaching an antivortex to a junction with vortex-induced JPS from Fig. 4(a). Thick and thin lines represent the image solution (circulating current mechanism) and the polar angle, Eq. (1), (stray-field mechanism) scaled to the same total JPS. It is seen that the difference between the two solutions is insignificant. Therefore, we will use Eq. (1), with V as a fitting parameter, for determination of vortex-induced JPS from experimental $I_c(H)$ patterns.

III. EXPERIMENTAL ANALYSIS

Planar proximity-coupled Josephson junctions of SNS-type (S—superconductor, N—normal metal) are made by cutting N/S bi-layers by a focused ion beam (FIB). The bilayer is deposited by magnetron sputtering. Films are first patterned into $L_x = 5$–6 μm wide bridges by photolithography and ion etching and subsequently cut by FIB. Finally, a vortex trap (a hole with diameter 30–50 nm) is made by FIB. We used various N metals: Cu, Fig. 5, a superparamagnetic CuNi alloy with approximately 50–50 concentration, Figs. 6, 7, and some other, all showing similar behavior. In all presented cases the thickness of N layer (Cu or CuNi) is $d_N = 50$ nm and S layer (Nb) is $d_S = 70$ nm. Measurements are done in a closed-cycle ^{4}He cryostat. Magnetic field is applied perpendicular to the film. More details about fabrication and characterization of such planar junctions (including device sketches) can be found in Refs. [17,27,43,53,58,59].

To study the mechanism of vortex-induced JPS we fabricated devices with vortex traps at different distances z_v from junctions and with correspondingly different polar angles Θ_v. AV can be manipulated (introduced or erased) by magnetic field and bias current [17,43]. We always start with the vortex-free state, obtained after zero-field cooling of the sample without bias current. A vortex is introduced in the trap by applying an appropriate current either at zero field or at small field below the lower critical field of the electrode, as described in Ref. [17]. Entrance/exit of AV results in an abrupt (instantaneous) change of the critical current. The two states with and without a vortex in the trap form steady and perfectly reproducible binary states [17]. This is how we can be sure that the vortex is indeed sitting in the trap. Only such reproducible states are shown and analyzed below. It could happen that eventually additional vortices enter junction electrodes and are placed randomly outside the trap. However this leads to irreversible and irreproducible states. If this happens, we clean the device by repeating the zero-field cooling procedure. For double-junction experiments, the position of the vortex can be unambiguously triangulated by simultaneous detection of responses in both junctions.

A. Single junction experiment

Figure 5(a) shows a scanning electron microscope (SEM) image of a Nb-Cu-Nb planar junction with a vortex trap. Device parameters are $L_x \simeq 5.25$ μm, $z_v \simeq 1.0$ μm, and $\Theta_v \simeq 0.77\pi$. Black lines in Fig. 5(b) represent measured vortex-free $I_c(H)$ modulation at $T = 2.5$ K. It has a Fraunhofer-type shape with a single central maximum at $H = 0$ [61]. Magenta lines in Fig. 5(b) represent $I_c(H)$ patterns after trapping a vortex at positive field. The $I_c(H)$ is significantly distorted:

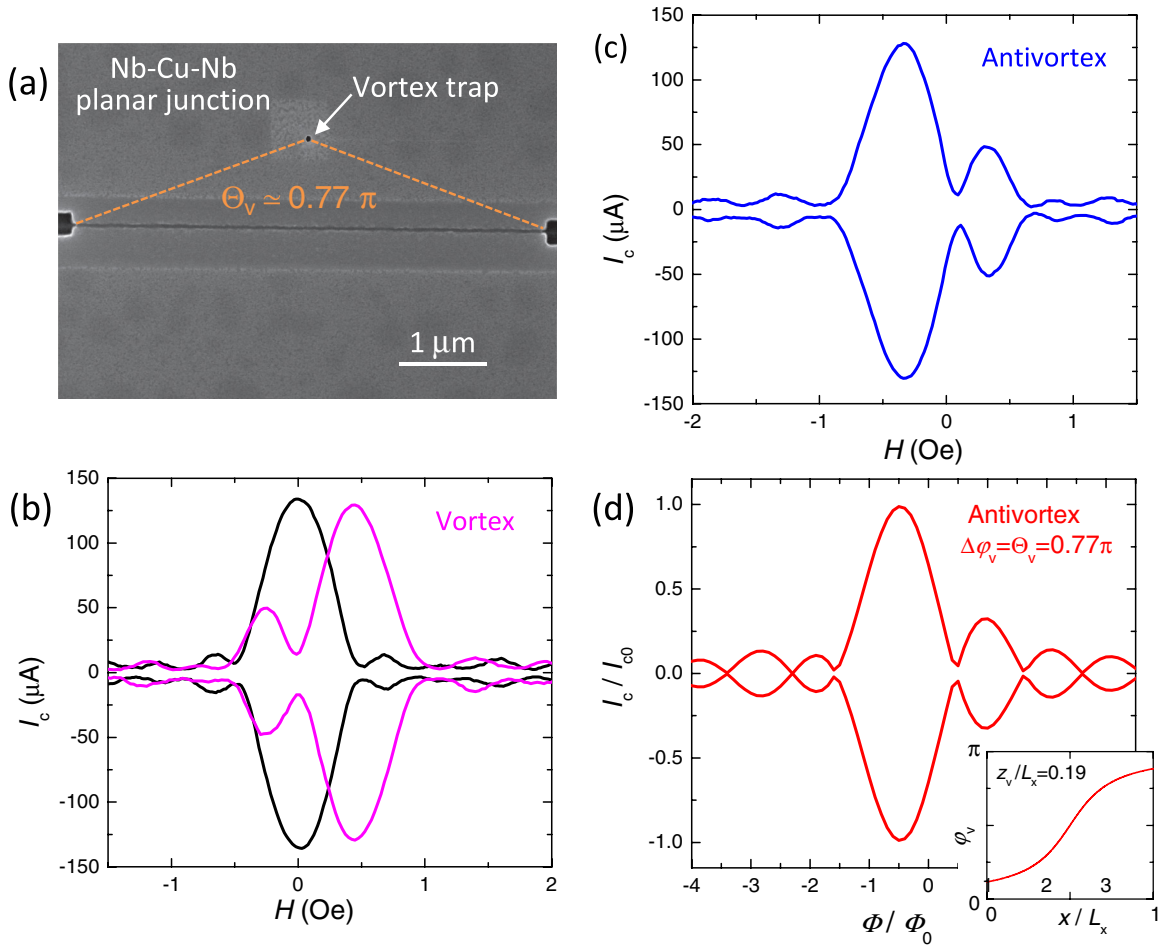

FIG. 5. Single junction experiment. (a) SEM image of a Nb-Cu-Nb planar junction with a vortex trap in the top electrode at $z_v = 1.0\ \mu$m from the junction, $z_v/L_x = 0.19$ and $\Theta_v = 0.77\pi$. (b) Measured $I_c(H)$ modulation without vortices (black lines) and with a trapped vortex (magenta lines). (c) $I_c(H)$ modulation with a trapped antivortex. It is mirror symmetric with respect to the vortex case in (b). (d) Calculated $I_c(H)$ pattern for the experimental geometry from (c). Inset shows corresponding antivortex-induced Josephson phase shift according to Eq. (1). A good agreement with experimental pattern in (c), without any fitting, indicates that the vortex-induced Josephson phase shift in this case is close to the vortex polar angle, $\Delta\varphi_v \simeq \Theta_v$.

The main maximum is shifted towards positive field and an additional secondary maximum appears at the left side. The shift of the main maximum in the direction of applied field is very characteristic for a trapped vortex [43]. Since the main maximum corresponds to $\Phi \simeq 0$, such a shift indicates that the effective vortex-induced field in the junction is opposite with respect to applied field, i.e., in Fig. 5(b) the vortex-induced flux is negative and a positive field is needed to compensate it to $\Phi = 0$, leading to the corresponding positive shift of the main $I_c(H)$ maximum. This is in contrast to $I_c(H)$ pattern shifts in ferromagnetic junctions, which trap flux of the same sign as applied field [60]. The reverse sign of vortex-induced field is consistent with stray fields, as sketched in Fig. 1(b). Figure 5(c) shows measured $I_c(H)$ pattern with a trapped antivortex. It is mirror symmetric with respect to the vortex case, Fig. 5(b).

In the device from Fig. 5, the vortex is placed at a rather large distance $z_v = 1\ \mu$m from the junction, which is significantly longer than both London, $\lambda \sim 100$–150 nm, and Pearl, $\lambda_P \sim 140$–320 nm, lengths. Therefore, as explained in Sec. II B, vortex stray fields should make a dominant contribution to JPS, which should be $\simeq\Theta_v$. Figure 5(d) represents numerically calculated $I_c(H)$ with antivortex-induced JPS according to Eq. (1) and with experimental $\Theta_v \simeq 0.77\pi$. Measured and calculated curves from Figs. 5(c) and 5(d) are in a quantitative agreement without any fitting [61]. This demonstrates that vortex-induced JPS scales with the polar angle, $|\Delta\varphi_v| \simeq \Theta_v$, for large $z_v \gg \lambda^*$, consistent with an earlier report [43].

B. Double junction experiment

As discussed in Sec. II, double junction experiments can provide crucial information about the mechanism of vortex-induced JPS. Therefore, we made samples, containing two planar JJs and vortex traps at different locations. First we consider the case when a vortex trap is placed in the middle electrode, shared by both junctions, as sketched in the inset of Fig. 2(c). In Fig. 6 we show results for such a device with two Nb-CuNi-Nb JJs. Figures 6(a) and 6(b) show vortex-free $I_c(H)$ patterns at $T = 6.6$ K. They have a regular Fraunhofer-type shape, indicating good uniformity of JJs [24].

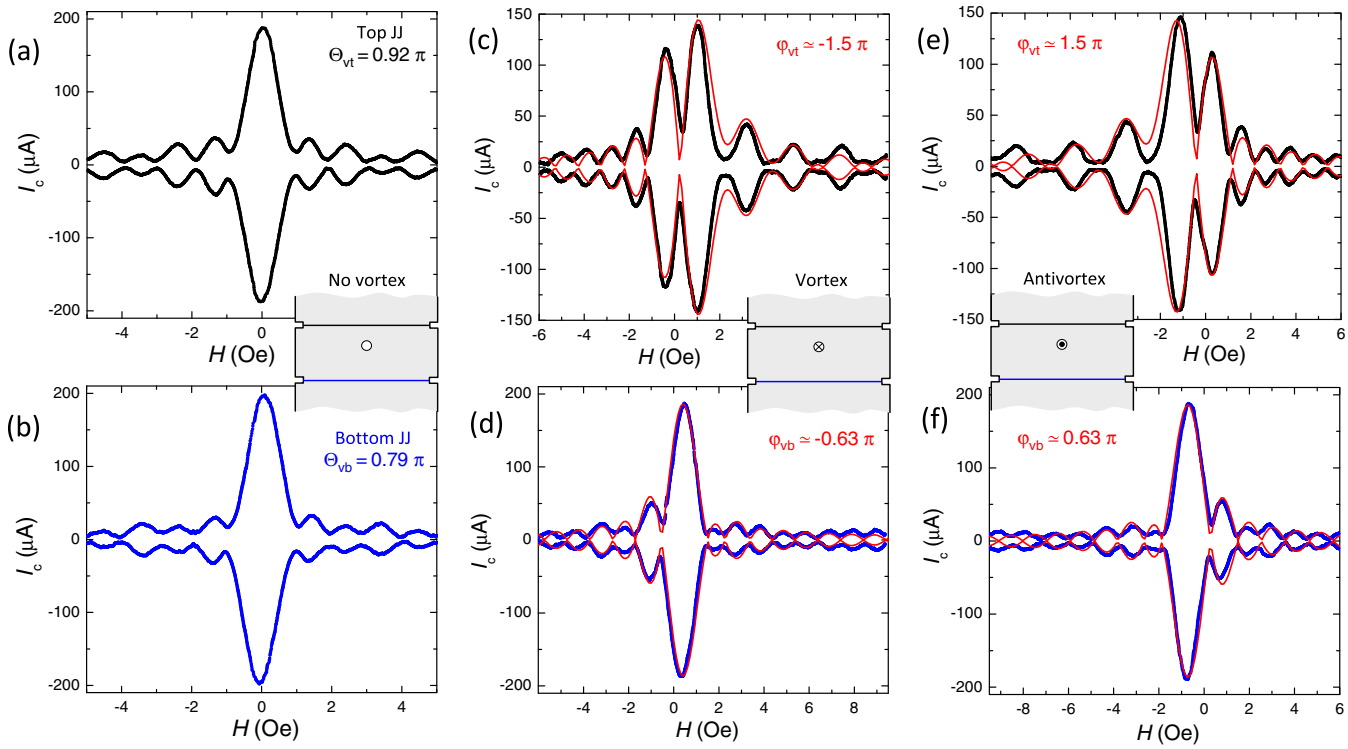

FIG. 6. Double junction experiment with a vortex trap in the middle electrode, placed closer to the top junction, $\Theta_{vt} = 0.92\pi$ and $\Theta_{vb} = 0.79\pi$. (a) and (b) Fraunhofer-type vortex free $I_c(H)$ patterns for both junctions. (c)–(f) Black and blue symbols represent measured $I_c(H)$ patterns after trapping [(c), (d)] a vortex [(e), (f)] an antivortex. Note that distortion is larger for the top junction [(c), (e)] which is closer to the vortex. Furthermore, vortex-induced JPS is larger than the polar angle for the top junction and smaller for the bottom junction, consistent with simulations in Fig. 2(c). Red lines represent numerical fits, used for estimation of JPS. Insets show sketches of experiments.

Junction lengths are $L_{xt} = 5.4\ \mu$m and $L_{xb} = 5.43\ \mu$m and separation between them $L_z \simeq 1.3\ \mu$m. The vortex trap is placed closer to the top JJ with $|z_{vt}| \simeq 0.36\ \mu$m (comparable to λ^*) and $z_{vb} \simeq 0.94\ \mu$m to the bottom JJ, as sketched in the inset. Corresponding polar angles are $\Theta_{vt} \simeq 0.92\pi$ and $\Theta_{vb} \simeq 0.79\pi$.

Black and blue symbols in Figs. 6(c) and 6(d) show measured $I_c(H)$ patterns for top and bottom junctions, respectively, after trapping a vortex. Figures 6(e) and 6(f) show $I_c(H)$ characteristics with a trapped antivortex. They are mirror symmetric with respect to vortex-induced characteristics from Figs. 6(c) and 6(d). From Figs. 6(c)–6(f) it is obvious that a vortex in the middle electrode distorts $I_c(H)$ patterns in both junctions, but the distortion is stronger in the top junction, which is closer to the vortex, consistent with simulations from Fig. 4. Thus, a double-junction geometry allows unambiguous triangulation of the vortex position.

Red lines in Figs. 6(c)–6(f) represent numerical fits. From those we obtain $|\Delta\varphi_{vt}| \simeq 1.5\pi$, which is significantly larger than $\Theta_{vt} \simeq 0.92\pi$ and $|\Delta\varphi_{vb}| \simeq 0.63\pi$, smaller than $\Theta_{vb} \simeq 0.79\pi$. This is inline with calculations for mesoscopic double-junction devices with finite-size L_z electrode, see Fig. 2(c): When the vortex is close to the top junction (small Θ_{vb}) the phase shift is concentrated in the top junction and becomes larger than Θ_{vt} up to a factor two for $z_{vt} \to 0$. However, this is accompanied by reduction of JPS in the furthermost bottom junction, compare dashed and solid lines in Fig. 2(c), qualitatively consistent with our observation.

C. The cutoff effect

Now we consider the case when the vortex is placed in outer electrodes of double-junction devices. Figure 7(a) shows a SEM picture of such a device. Junction lengths are $L_{xt} = 5.58\ \mu$m and $L_{xb} = 5.56\ \mu$m. The separation between junctions was made intentionally small 0.6 μm, so that polar angles to both junctions are not very different. Vortex-free characteristics for both junctions at $T = 6.7$ K are shown in Fig. 7(b). They have regular Fraunhofer-type shapes with minor distortions [61].

Initially, a single vortex trap was made in the top electrode close to the top junction, marked as the top trap in Fig. 7(a). The corresponding distances to the top and the bottom junction are $z_{vt} = 0.38\ \mu$m and $z_{vb} = 1.0\ \mu$m. Polar angles are almost the same as in Fig 6: $\Theta_{vt} \simeq 0.91\pi$ and $\Theta_{vb} \simeq 0.78\pi$. However, the result of vortex trapping is quite different.

Figures 7(c) and 7(d) show $I_c(H)$ patterns for the top and bottom junctions, respectively, with a trapped antivortex in the top trap at $T \simeq 6.7$ K. It is seen that $I_c(H)$ in the top junction is strongly distorted. Red lines in panel (c) represent a numerical fit, which yields $\Delta\varphi_{vt} = 1.55\pi > \Theta_{vt}$. However, in the bottom junction there is no visible distortion with respect to the vortex-free case $\Delta\varphi_{vb} \simeq 0$. Consequently, the vortex in the top electrode does not induce a sensible JPS in the bottom junction despite a large polar angle $\Theta_{vb} = 0.78\pi$.

After this measurement the sample was taken back to FIB and a second trap was made in the bottom electrode. The bottom trap, marked in Fig. 7(a), was made at the

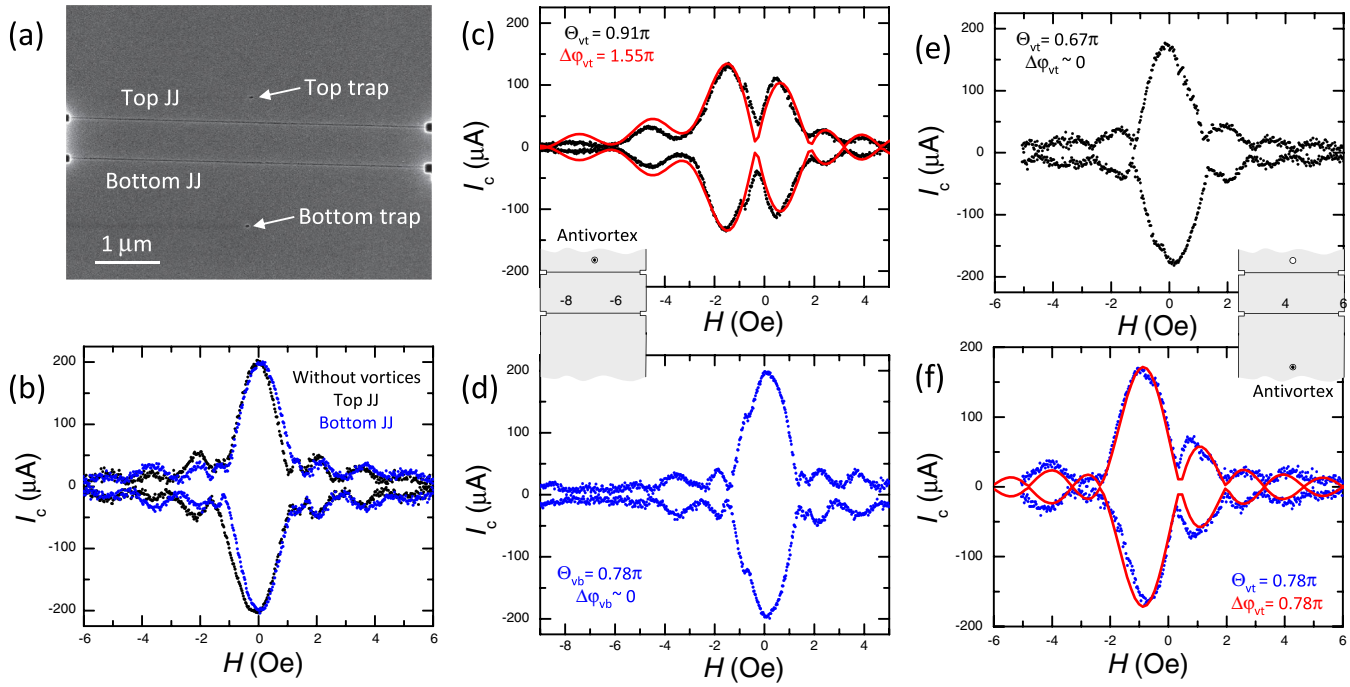

FIG. 7. Experimental demonstration of the cutoff effect for a double-junction device with vortex traps in outmost electrodes. (a) SEM image of the device with two nearby Nb-CuNi-Nb junctions. (b) Vortex-free $I_c(H)$ patterns for both junctions. (c) and (d) $I_c(H)$ patterns for the top (c) and bottom (d) junctions with a trapped antivortex in the top trap (this is the only trap at this state of the sample, as sketched in the inset). Note that the $I_c(H)$ pattern for the top junction is strongly distorted, indicating the large total JPS $\Delta\varphi_v = 1.55\pi$ as seen from the numerical fit (red line) in (c). However, the pattern in the bottom junction is practically unaffected. (e) and (f) Measurements after making a second bottom trap at the same distance to the bottom junction as for the top trap, see the sketch. Symbols represent $I_c(H)$ patterns with an antivortex in the bottom trap. This time the pattern in the bottom junction is significantly distorted but in the top junction is not. This illustrates that the vortex-induced JPS is terminated at the junction and does not persist beyond it.

same distance and polar angle to the bottom junction as the top trap, $|z_{vb}| = 1.0\ \mu$m, $\Theta_{vb} = 0.78\pi$. Corresponding values for the top junction are $|z_{vt}| = 1.6\ \mu$m and $\Theta_{vt} = 0.67\pi$. Figures 7(e) and 7(f) show $I_c(H)$ modulation for top and bottom junctions with a trapped antivortex in the bottom trap. It is seen that $I_c(H)$ in the bottom junction, which shares one electrode with the vortex, is now significantly distorted. A numerical fit, shown by red lines in Figs. 7(f), yields $\Delta\varphi_{vb} = 0.78\pi$, equal to the corresponding polar angle Θ_{vb}. However, now the top junction, which has vortex-free electrodes, is unaffected, $\Delta\varphi_{vt} \simeq 0$.

Observations from Fig. 7 clearly demonstrate that vortex-induced JPS is cutoff by the nearest junction and does not persist beyond it. JPS is induced only when AV is placed in one of the junction electrodes and is not observed otherwise, irrespective of the distance between the vortex and the junction (at least for $z_v > \lambda$ [62]). The cutoff makes it evident that JPS is not due to the Aharonov-Bohm effect. On the other hand, the cutoff is expected for both JPS mechanisms, discussed in Secs. II A and II B. The current-induced JPS is terminated because vortex currents do not cross the junction [57]. The stray-field JPS is terminated due to almost complete closing of field lines through the nearest junction, see Fig. 3(c).

D. Distance dependence of the phase shift

From presented data it follows that vortex-induced JPS can be equal [Figs. 5 and 7(f)], larger [Figs. 6(c) and 6(e) and 7(c)], or smaller [Figs. 6(d) and 6(f)] than the polar angle Θ_v. Since junction lengths L_x are approximately the same, factors that control JSP are the vortex-junction distance z_v and the electrode size L_z, which is finite for the case when vortices are placed in middle electrodes of double-junction devices and essentially infinite otherwise.

Figure 8 summarizes the dependence of observed JPS on the vortex polar angle. Blue symbols represent previously reported data from Ref. [43]. Red symbols represent data from this study. Filled red circles correspond to $L_z \sim \infty$, either for single-junction devices or double-junction devices with the vortex in outmost electrodes. Open red symbols represent double-junction data for the vortex in the middle electrode with finite L_z. Similar symbols represent JPS for junctions on the same device. For example, open squares represent data from Fig. 6. JPS values $\Delta\varphi_v$ are obtained from fitting using Eq. (1), as shown in Figs. 5–7. The accuracy of determination of $\Delta\varphi_v$ is limited mostly by some deviations of vortex-free $I_c(H)$ from the pure Fraunhofer pattern [61]. It may also be affected by the presence of far-away vortices (at $z_v \gtrsim L_x$) that may create a small irregular distortion of $I_c(H)$, which is difficult to control just because of its smallness. We estimate the corresponding systematic uncertainty less than 0.1π. The solid black line in Fig. 8 represents Eq. (1) with linear dependence $\Delta\varphi_v = \Theta_v$, expected for the stray-field mechanism in macroscopic devices. Dashed lines represent current-induced image solutions for mesoscopic devices. Olive and

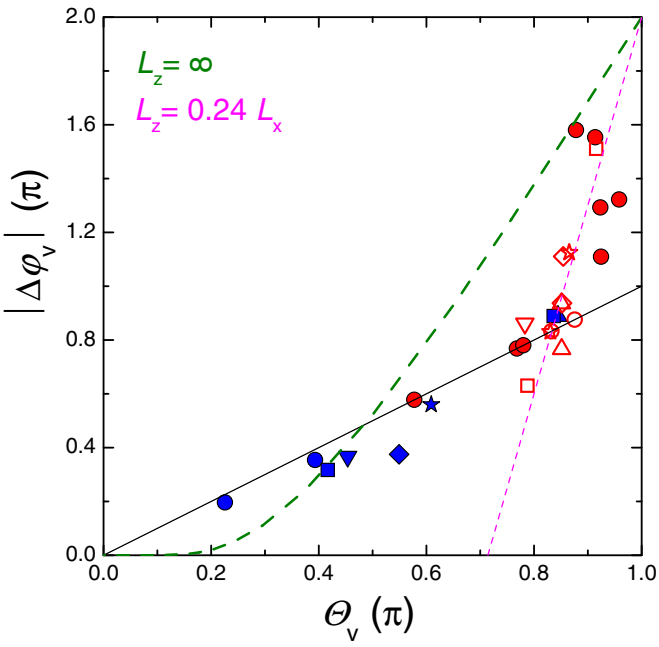

FIG. 8. Vortex-induced JPS as a function of vortex polar angle. Red symbols are from the present study and blue from Ref. [43]. Solid circles are for single- and double-junction devices with vortices in outmost electrodes, $L_z = \infty$. Open symbols are for double-junction devices with the vortex in the middle electrode with finite L_z. Similar symbols correspond to junctions at the same device. Solid and dashed lines represent stray-field, Eq. (1), and current-induced image solutions ($L_z = \infty$, olive and $L_z = 0.24L_x$, magenta curve), respectively. A crossover from linear to superlinear dependence occurs at $\Theta_v \gtrsim 0.9\pi$, corresponding to $z_v \lesssim 500$ nm $\sim\lambda^*$. The crossover indicates transition in the mechanism of the phase shift from stray-field-induced (linear) at large distances $z_v \gg \lambda^*$ to circulating-current-induced (superlinear) at a short range $z_v \lesssim \lambda^*$.

magenta dashed lines correspond to $L_z \sim \infty$ and $L_z = 0.24L_x$, respectively.

From Fig. 8 it is seen that for small Θ_v (large distances) JSV scales linearly with the polar angle $\Delta\varphi_v \simeq \Theta_v$. However at larger Θ_v (small z_v), the phase shift becomes larger than the polar angle (superlinear) and approaches 2π, qualitatively consistent with the image solution [62]. The upturn is more abrupt than predicted by the $L_z = \infty$ solution (olive dashed line). This may have two reasons. First, for finite L_z (middle electrode), $\Delta\varphi_v$ vs Θ_v line is steeper because the minimal Θ_v is finite, cf. Figs. 2(b) and 2(c). Magenta dashed line in Fig. 8 represents the image solution for $L_z = 0.24L_x$, corresponding to the device from Fig. 6 with $L_z = 1.3$ μm. It provides a seemingly good description of data for the vortex in the middle electrode (open symbols). In concord with such a description, some of the open red symbols lie below the $\Delta\varphi_v = \Theta_v$ line. Those points correspond to farmost JJs in double junction devices, as in Figs. 6(d) and 6(f). Such a deviation is expected for the current-induced mechanism due to concentration of JPS at the nearest to the vortex junction, see Fig. 2(c).

On the other hand, from Fig. 8 it is seen that even for vortices in outer electrodes (solid symbols) the upturn $\Delta\varphi_v(\Theta_v)$ follows approximately the same line. Consequently there should be a more general reason for the upturn, unrelated to L_z. The origin becomes clear if we consider the upturn as a crossover from a linear stray-field induced JPS at large distances to a superlinear $\Delta\varphi_v(\Theta_v)$ for current-induced JPS at small distances. Such a crossover should occur at $z_v \sim \lambda^*$, which separates ranges of validity of the two mechanisms. Indeed, the upturn $\Delta\varphi_v(\Theta_v)$ starts at distances $z_v \lesssim 500$ nm, which is comparable to the estimated value of the Pearl length $\lambda_P \simeq 300$ nm. Therefore, we conclude that the observed linear to superlinear crossover is primarily due to a gradual transition from the long-range stray-field mechanism at large distances $z_v \gg \lambda^*$ to a short-range circulating current mechanism at $z_v \lesssim \lambda^*$. Thus we identify two distinct mechanisms of Josephson phase shift generation by an Abrikosov vortex. This is our main result.

IV. CONCLUSIONS

To summarize, we performed a systematic study of Abrikosov vortex-induced phase shifts in planar Josephson junctions. We demonstrated that JPS depends on the polar angle of the vortex within the junction and decays slowly, in a long-range manner, approximately inversely proportionally to the distance. Thus a significant phase shift can be generated even at very large distances (few microns), compared to the London penetration depth $\lambda \simeq 100$ nm. However, experiments with two consecutive junctions have shown that vortex-induced JPS is cutoff by the nearest junction and does not persist beyond it, irrespective of the distance. Thus, this is not a true long-range phenomenon, like the Aharonov-Bohm effect. The phase shift is induced only when the vortex is present in one of the junction electrodes. On a quantitative level we observed a crossover from a linear dependence $\Delta\varphi_v \simeq \Theta_v$ at large distances $z_v \gg \lambda^*$ to a superlinear dependence at shorter distances $z_v \lesssim \lambda^*$.

We performed theoretical and numerical analysis of two mechanisms of vortex-induced JPS generation: By circulating vortex currents at a short range $r \lesssim \lambda^*$ and by vortex stray fields at a long range $r \gg \lambda^*$. For the current-induced mechanism we derived a simple and rigorous image array solution, valid for finite-size electrodes both for Abrikosov and Pearl vortices. We emphasize that the two mechanisms are distinct and independent. Vortex stray fields spread *outside* a superconductor and can generate JPS at arbitrary long distances $r \gg \lambda^*$, at which there are no circulating vortex currents *inside* a superconductor. Similarly, circulating vortex currents create a large phase shift only at a short-range $r < \lambda^*$, where circulating current densities are large. In the mesoscopic case it occurs without involvement of magnetic fields.

Observation of the linear-to-superlinear crossover $\Delta\varphi_v(\Theta_v)$ clearly revealed gradual transition from one mechanism to another. Altogether this work provides a comprehensive quantitative description of the vortex induced Josephson phase shift. We anticipate that this knowledge can be employed for development of future generation of compact Josephson electronic devices like memory [17] and tunable phase shifters. Both compactness and tunability are facilitated by the small size of the Abrikosov vortex, $\lambda \sim 100$ nm, which represents the smallest magnetic object in a superconductor.

ACKNOWLEDGMENTS

The work was accomplished during a sabbatical period of V.M.K. at Moscow Institute of Physics and Technology and was supported by the Russian Science Foundation, Grant No. 19-19-00594, and the 5-top-100 program at MIPT.

APPENDIX A: IMAGE ARRAY SOLUTION

Let us consider a vortex ($V = 1$) at position (x_v, z_v) in the electrode-1 with sizes (L_x, L_z), as sketched in Fig. 2(a). We assume that at least one of the sizes is mesoscopic, $L_x \ll \lambda^*$. Mirror reflections from the vertical (left-right) edges will create a first image row [marked I in Fig. 2(a)] at $z_1 = z_v$ with antivortices at $x_{n-} = -2(n-1)L_x - x_v$ and $x_{n+} = 2nL_x - x_v$, $(n = 1, 2, 3...)$ and vortices at $x_{m-} = -2mL_x + x_v$ and $x_{m+} = 2mL_x + x_v$, $(m = 1, 2, 3...)$. Each of them induces a phase shift according to Eq. (1). The original vortex will create a total phase shift $\Delta\varphi_0 = \arctan[(L_x - x_v)/z_v] + \arctan[x_v/z_v]$. The two primary antivortex images [marked green in Fig. 2(a)] will reduce it by $\Delta\varphi_1 = -\arctan[(L_x + x_v)/z_v] + \arctan[x_v/z_v] - \arctan[(2L_x - x_v)/z_v] + \arctan[(L_x - x_v)/z_v]$. Subsequent vortex and antivortex pairs will add $\Delta\varphi_m = \arctan[((2m+1)L_x - x_v)/z_v] - \arctan[(2mL_x - x_v)/z_v] + \arctan[(2mL_x + x_v)/z_v] - \arctan[((2m-1)L_x + x_v)/z_v]$ and $\Delta\varphi_{m+1} = -\arctan[((2m+1)L_x + x_v)/z_v] + \arctan[(2mL_x + x_v)/z_v] - \arctan[(2m+2)L_x - x_v)/z_v] - \arctan[((2m+1)L_x + x_v)/z_v]$, $(m = 1, 2, 3...)$, correspondingly. As a result, the total phase shift induced by row I can be written as

$$\Delta\varphi_{\rm I} = 2\left(\tan^{-1}\frac{x_v}{z_v} - \sum_{n=1}^{\infty}\left[\tan^{-1}\frac{2nL_x - x_v}{z_v} - \tan^{-1}\frac{(2n-1)L_x - x_v}{z_v} - \tan^{-1}\frac{2nL_x + x_v}{z_v} + \tan^{-1}\frac{(2n-1)L_x + x_v}{z_v}\right]\right). \quad \text{(A1)}$$

If electrode 1 is semi-infinite $L_z = \infty$, then we need to add only one additional image row from the bottom (junction) edge, marked I′ in Fig. 2(a). It is obvious that this row will create exactly the same phase shift, as row I. Consequently, for a semi-infinite electrode the total phase shift is double the phase shift of the primary row.

$$\Delta\varphi_v(L_z = \infty) = 2\Delta\varphi_{\rm I}. \quad \text{(A2)}$$

For a finite-size electrode additional image rows appear due to mirror reflections from the top edge, as depicted in Fig. 2(a). Reflection of the primary row I from the top edge leads to the secondary antirow II $z = 2L_z - z_v$. Its reflection from the bottom edge leads to a row II′ at $z = -2L_z + z_v$, and so on. Each image vortex in the row generates a phase shift according to Eq. (1) with corresponding coordinates (x_n, z_m). Similar to the case of antivortices and vortices in the primary row I, antirows appear at $z_{n-} = -2(n-1)L_z - z_v$ and $z_{n+} = 2nL_z - z_v$, $(n = 1, 2, 3...)$, rows at $z_{m-} = -2mL_z + z_v$ and $z_{m+} = 2mL_z + z_v$, $(m = 1, 2, 3...)$ and couples of rows are symmetric with respect to the junction [e.g., rows I–I′ and II–II′ in Fig. 2(a)] and create identical phase shifts. This simplifies calculations.

The sum in Eq. (A1) is well behaving and converges at $n = 10$–20, depending on z_v. The larger is z_v (small Θ_v) the more terms are needed. $n = 10$ is enough for achieving an absolute accuracy $\lesssim 0.01\pi$. The simulated curves shown in Fig. 2(b) were obtained with 20 terms and absolute accuracy $\lesssim 0.001\pi$. For a finite L_z, Θ_v cannot be small and, therefore, convergence is much faster. Data shown in Fig. 2(a) for finite L_z was obtained by summing four pairs of rows, but already three rows provide a similar result with no visible difference at the scale of the graph.

APPENDIX B: COMPARISON WITH CLEM'S SOLUTION

In Ref. [44] Clem obtained a self-consistent solution for JPS induced by a Pearl vortex in a thin film planar JJ with narrow, long electrodes using a conformal mapping method:

$$\varphi_{Pearl} = \arg\left[\frac{w(\zeta) - w^*(\zeta_v)}{w(\zeta_v) - w(\zeta)}\right], \quad \text{(B1)}$$

where $\zeta = x + iz$, $\zeta_v = x_v + iz_v$, $w(\zeta) = i\sinh(\pi\zeta/L_x)$ and w^* is a complex conjugate of w. The solution is valid for a junction with $d \ll \lambda$, $L_x \ll \lambda_P$ and $L_z = \infty$. The solution is represented by the dashed magenta line in Fig. 2(b).

[1] G. Blatter, V. B. Geshkenbein, and L. B. Ioffe, Design aspects of superconducting-phase quantum bits, Phys. Rev. B **63**, 174511 (2001).

[2] T. Ortlepp, Ariando, O. Mielke, C. J. M. Verwijs, K. F. K. Foo, H. Rogalla, F. H. Uhlmann, and H. Hilgenkamp, Flip-flopping fractional flux quanta, Science **312**, 1495 (2006).

[3] A. K. Feofanov, V. A. Oboznov, V. V. Bol'ginov, J. Lisenfeld, S. Poletto, V. V. Ryazanov, A. N. Rossolenko, M. Khabipov, D. Balashov, A. B. Zorin, P. N. Dmitriev, V. P. Koshelets, and A. V. Ustinov, Implementation of superconductor/ferromagnet/superconductorpi-shifters in superconducting digital and quantum circuits, Nat. Phys. **6**, 593 (2010).

[4] I. I. Soloviev, N. V. Klenov, S. V. Bakurskiy, M. Yu. Kupriyanov, A. L. Gudkov, and A. S. Sidorenko, Beyond Moore's technologies: Operation principles of a superconductor alternative, Beilstein J. Nanotechnol. **8**, 2689 (2017).

[5] M. Neeley, M. Ansmann, R. C. Bialczak, M. Hofheinz, N. Katz, E. Lucero, A. O'Connell, H. Wang, A. N. Cleland, and J. M. Martinis, Transformed dissipation in superconducting quantum circuits, Phys. Rev. B **77**, 180508(R) (2008).

[6] S. Gladchenko, D. Olaya, E. Dupont-Ferrier, B. Douçot, L. B. Ioffe, and M. E. Gershenson, Superconducting nanocircuits for topologically protected qubits, Nat. Phys. **5**, 48 (2009).

[7] J. B. Majer, J. B. Butcher, and J. E. Mooij, Simple phase bias for superconducting circuits, Appl. Phys. Lett. **80**, 3638 (2002).

[8] M. Wulf, T. A. Ohki, and M. J. Feldman, A simple circuit to supply constant flux biases for superconducting quantum computing, J. Phys. Conf. Ser. **43**, 1397 (2006).

[9] L. Longobardi, S. Pottorf, V. Patel, and J. E. Lukens, Development and testing of a persistent flux bias for qubits, IEEE Trans. Appl. Supercond. **17**, 88 (2007).

[10] F. G. Paauw, A. Fedorov, C. J. P. M. Harmans, and J. E. Mooij, Tuning the Gap of a Superconducting Flux Qubit, Phys. Rev. Lett. **102**, 090501 (2009).

[11] X. Zhu, A. Kemp, S. Saito, and K. Semba, Coherent operation of a gap-tunable flux qubit, Appl. Phys. Lett. **97**, 102503 (2010).

[12] A. Fedorov, P. Macha, A. K. Feofanov, C. J. P. M. Harmans, and J. E. Mooij, Tuned Transition from Quantum to Classical for Macroscopic Quantum States, Phys. Rev. Lett. **106**, 170404 (2011).

[13] M. J. Schwarz, J. Goetz, Z. Jiang, T. Niemczyk, F. Deppe, A. Marx, and R. Gross, Gradiometric flux qubits with a tunable gap, New J. Phys. **15**, 045001 (2013).

[14] H. Deng, Y. Wu, Y. Zheng, N. Akhtar, J. Fan, X. Zhu, J. Li, Y. Jin, and D. Zheng, Working point adjustable dc-squid for the readout of gap tunable flux qubit, IEEE Trans. Appl. Supercond. **25**, 1602504 (2015).

[15] D. Balashov, B. Dimov, M. Khabipov, T. Ortlepp, D. Hagedorn, A. B. Zorin, F.-I. Buchholz, F. H. Uhlmann, and J. Niemeyer, Passive Phase Shifter for Superconducting Josephson Circuits, IEEE Trans. Appl. Supercond. **17**, 142 (2007).

[16] B. Dimov, D. Balashov, M. Khabipov, T. Ortlepp, F.-I. Buchholz, A. B. Zorin, J. Niemeyer, and F. H. Uhlmann, Implementation of superconductive passive phase shifters in high-speed integrated RSFQ digital circuits, Supercond. Sci. Technol. **21**, 045007 (2008).

[17] T. Golod, A. Iovan, and V. M. Krasnov, Single Abrikosov vortices as quantized information bits, Nat. Commun. **6**, 8628 (2015).

[18] S. V. Bakurskiy, N. V. Klenov, I. I. Soloviev, M. Yu. Kupriyanov, and A. A. Golubov, Superconducting phase domains for memory applications, Appl. Phys. Lett. **108**, 042602 (2016).

[19] V. I. Zdravkov, D. Lenk, R. Morari, A. Ullrich, G. Obermeier, C. Müller, H.-A. Krug von Nidda, A. S. Sidorenko, S. Horn, R. Tidecks, and L. R. Tagirov, Memory effect and triplet pairing generation in the superconducting exchange biased Co/CoOx/Cu41Ni59/Nb/Cu41Ni59 layered heterostructure, Appl. Phys. Lett. **103**, 062604 (2013).

[20] E. Goldobin, H. Sickinger, M. Weides, N. Ruppelt, H. Kohlstedt, R. Kleiner, and D. Koelle, Memory cell based on a ȷ Josephson junction, Appl. Phys. Lett. **102**, 242602 (2013).

[21] B. Baek, W. H. Rippard, S. P. Benz, S. E. Russek, and P. D. Dresselhaus, Hybrid superconducting-magnetic memory device using competing order parameters, Nat. Commun. **5**, 3888 (2014).

[22] B. M. Niedzielski, T. J. Bertus, J. A. Glick, R. Loloee, W. P. Pratt, Jr., and N. O. Birge, Spin-valve Josephson junctions for cryogenic memory, Phys. Rev. B **97**, 024517 (2018).

[23] R. Fehrenbacher, V. B. Geshkenbein, and G. Blatter, Pinning phenomena and critical currents in disordered long Josephson junctions, Phys. Rev. B **45**, 5450 (1992).

[24] V. M. Krasnov, V. A. Oboznov, and N. F. Pedersen, Fluxon dynamics in long Josephson junctions in the presence of a temperature gradient or spatial nonuniformity, Phys. Rev. B **55**, 14486 (1997).

[25] T. Gaber, E. Goldobin, A. Sterck, R. Kleiner, D. Koelle, M. Siegel, and M. Neuhaus, Nonideal artificial phase discontinuity in long Josephson 0-κ junctions, Phys. Rev. B **72**, 054522 (2005).

[26] M. Alidoust and J. Linder, φ-state and inverted Fraunhofer pattern in nonaligned Josephson junctions, Phys. Rev. B **87**, 060503 (2013).

[27] T. Golod, O. M. Kapran, and V. M. Krasnov, Planar Superconductor-Ferromagnet-Superconductor Josephson Junctions as Scanning-Probe Sensors, Phys. Rev. Appl. **11**, 014062 (2019).

[28] B. Chesca, D. John, R. Pollett, M. Gaifullin, J. Cox, C. J. Mellor, and S. Savel'ev, Magnetic field tunable vortex diode made of $YBa_2Cu_3O_{7-\delta}$ Josephson junction asymmetrical arrays, Appl. Phys. Lett. **111**, 062602 (2017).

[29] V. V. Ryazanov, V. A. Oboznov, A. Yu. Rusanov, A. V. Veretennikov, A. A. Golubov, and J. Aarts, Coupling of Two Superconductors through a Ferromagnet: Evidence for a π Junction, Phys. Rev. Lett. **86**, 2427 (2001).

[30] T. Kontos, M. Aprili, J. Lesueur, F. Genet, B. Stephanidis, and R. Boursier, Josephson Junction through a Thin Ferromagnetic Layer: Negative Coupling, Phys. Rev. Lett. **89**, 137007 (2002).

[31] H. Sellier, C. Baraduc, F. Lefloch, and R. Calemczuk1, Half-Integer Shapiro Steps at the 0-π Crossover of a Ferromagnetic Josephson Junction, Phys. Rev. Lett. **92**, 257005 (2004).

[32] D. J. Van Harlingen, Phase-sensitive tests of the symmetry of the pairing state in the high-temperature superconductors: Evidence for $d_{x^2-y^2}$ symmetry, Rev. Mod. Phys. **67**, 515 (1995).

[33] C. C. Tsuei and J. R. Kirtley, Pairing symmetry in cuprate superconductors, Rev. Mod. Phys. **72**, 969 (2000).

[34] Y. Ota, M. Machida, T. Koyama, and H. Matsumoto, Theory of Heterotic Superconductor-Insulator-Superconductor Josephson Junctions between Single- and Multiple-Gap Superconductors, Phys. Rev. Lett. **102**, 237003 (2009).

[35] J. Linder, I. B. Sperstad, and A. Sudbø, $0-\pi$ phase shifts in Josephson junctions as a signature for the $s_{\pm}$-wave pairing state, Phys. Rev. B **80**, 020503(R) (2009).

[36] A. E. Koshelev, Phase diagram of Josephson junction between s and $s_{\pm}$ superconductors in the dirty limit, Phys. Rev. B **86**, 214502 (2012).

[37] A. A. Kalenyuk, A. Pagliero, E. A. Borodianskyi, A. A. Kordyuk, and V. M. Krasnov, Phase-Sensitive Evidence for the Sign-Reversal $s_{\pm}$ Symmetry of the Order Parameter in an Iron-Pnictide Superconductor Using Nb/$Ba_{1-x}Na_xFe_2As_2$ Josephson Junctions, Phys. Rev. Lett. **120**, 067001 (2018).

[38] A. Buzdin and A. E. Koshelev, Periodic alternating 0- and π-junction structures as realization of φ-Josephson junctions, Phys. Rev. B **67**, 220504(R) (2003).

[39] H. Sickinger, A. Lipman, M. Weides, R. G. Mints, H. Kohlstedt, D. Koelle, R. Kleiner, and E. Goldobin, Experimental Evidence of a φ Josephson Junction, Phys. Rev. Lett. **109**, 107002 (2012).

[40] F. Konschelle, I. V. Tokatly, and F. S. Bergeret, Theory of the spin-galvanic effect and the anomalous phase shift φ_0 in superconductors and Josephson junctions with intrinsic spin-orbit coupling, Phys. Rev. B **92**, 125443 (2015).

[41] L. G. Aslamazov and E. V. Gurovich, Pinning of solitons by Abrikosov vortices in distributed Josephson junctions, JETP Lett. **40**, 746 (1984).

[42] A. Gurevich and L. D. Cooley, Anisotropic flux pinning in a network of planar defects, Phys. Rev. B **50**, 13563 (1994).

[43] T. Golod, A. Rydh, and V. M. Krasnov, Detection of the Phase Shift from a Single Abrikosov Vortex, Phys. Rev. Lett. **104**, 227003 (2010).

[44] J. R. Clem, Effect of nearby Pearl vortices upon the Ic versus B characteristics of planar Josephson junctions in thin and narrow superconducting strips, Phys. Rev. B **84**, 134502 (2011).

[45] V. G. Kogan and R. G. Mints, Interaction of Josephson junction and distant vortex in narrow thin-film superconducting strips, Phys. Rev. B **89**, 014516 (2014).

[46] S. Mironov, E. Goldobin, D. Koelle, R. Kleiner, Ph. Tamarat, B. Lounis, and A. Buzdin, Anomalous Josephson effect controlled by an Abrikosov vortex, Phys. Rev. B **96**, 214515 (2017).

[47] M. V. Milošević, A. Kanda, S. Hatsumi, F. M. Peeters, and Y. Ootuka, Local Current Injection into Mesoscopic Superconductors for the Manipulation of Quantum States, Phys. Rev. Lett. **103**, 217003 (2009).

[48] J. Sok and D. K. Finnemore, Thermal depinning of a single superconducting vortex in Nb, Phys. Rev. B **50**, 12770 (1994).

[49] I. S. Veshchunov, W. Magrini, S. V. Mironov, A. G. Godin, J.-B. Trebbia, A. I. Buzdin, Ph. Tamarat, and B. Lounis, Optical manipulation of single flux quanta, Nat. Commun. **7**, 12801 (2016).

[50] Y. Aharonov and D. Bohm, Significance of Electromagnetic Potentials in the Quantum Theory, Phys. Rev. **115**, 485 (1959).

[51] J. Pearl, Current distribution in superconducting films carrying quantized fluxoids, Appl. Phys. Lett. **5**, 65 (1964).

[52] V. M. Krasnov and D. Winkler, Static and dynamic properties of stacked Josephson junctions: Analytic solution, Phys. Rev. B **56**, 9106 (1997).

[53] A. A. Boris, A. Rydh, T. Golod, H. Motzkau, A. M. Klushin, and V. M. Krasnov, Evidence for Nonlocal Electrodynamics in Planar Josephson Junctions, Phys. Rev. Lett. **111**, 117002 (2013).

[54] V. G. Kogan, V. V. Dobrovitski, J. R. Clem, Y. Mawatari, and R. G. Mints, Josephson junction in a thin film, Phys. Rev. B **63**, 144501 (2001).

[55] M. Moshe, V. G. Kogan, and R. G. Mints, Edge-type Josephson junctions in narrow thin-film strips, Phys. Rev. B **78**, 020510(R) (2008).

[56] J. R. Clem, Josephson junctions in thin and narrow rectangular superconducting strips, Phys. Rev. B **81**, 144515 (2010).

[57] We assume that the Josephson current density is negligible with respect to the circulating current density in the vortex $J_c \ll J_v$, which is easily satisfied in the considered limit $z_v \ll \lambda^*$ due to divergence of Eq. (8) in the vortex center.

[58] V. M. Krasnov, O. Ericsson, S. Intiso, P. Delsing, V. A. Oboznov, A. S. Prokofiev, and V. V. Ryazanov, Planar S-F-S Josephson junctions made by focused ion beam etching, Physica C **418**, 16 (2005).

[59] V. M. Krasnov, T. Golods, and T. Bauch, and P. Delsing, Anticorrelation between temperature and fluctuations of the switching current in moderately damped Josephson junctions, Phys. Rev. B **76**, 224517 (2007).

[60] A. Iovan, T. Golod, and V. M. Krasnov, Controllable generation of a spin-triplet supercurrent in a Josephson spin valve, Phys. Rev. B **90**, 134514 (2014).

[61] Small misfits between experimental and theoretical $I_c(H)$ curves can be attributed to slight deviations of vortex-free $I_c(H)$ from the pure Fraunhofer pattern. Most likely, this reflects minor nonuniformity of critical current distribution within junctions [24].

[62] For $z_v \lesssim 100$ nm $\simeq \lambda$ we were not able to reproducibly place a vortex in the trap, most likely because the attractive force to the junction edge (the antivortex image) exceeds the pinning force. This is not surprising because the current density at the distance $r \lesssim \lambda$ from the vortex is a significant fraction of the depairing current and may well exceed the depinning current density from the trap.